

## Research Paper

# Improving inner structure and properties of additive manufactured amorphous plastic parts: The effects of extrusion nozzle diameter and layer height



Dirk Fischer, Claudia Eßbach, Robert Schönherr, Dagmar Dietrich, Daniela Nickel\*

Berufsakademie Sachsen – Staatliche Studienakademie Glauchau, University of Cooperative Education, Kopernikusstrasse 51, 08371 Glauchau, Germany

## ARTICLE INFO

## ABSTRACT

**Keywords:**

Additive manufacturing – Fused Filament Fabrication  
Acrylonitrile butadiene styrene (ABS)  
Porosity  
Mechanical strength  
Crazing

Material extrusion is an efficient additive manufacturing process for thermoplastic materials in the field of rapid prototyping, rapid tooling, rapid manufacturing and rapid repair. Parts to be additive manufactured of acrylonitrile butadiene styrene (ABS Terluran GP 35) with mechanical properties close to the data sheet specification of injection molded parts are in the focus of this study. An in-house process chain from the plastic pellets to the finished additive manufactured product is developed to monitor and to define the process parameters for each individual processing step using the terpolymer. By varying the parameters extrusion nozzle diameter and layer height, the production-related internal part structure and the surface topography of the additive manufactured tensile test specimens are improved in such a way that the mechanical property yield strength rises from 55% to 75% of the data sheet specification for injection molded ABS parts. The elongation at break increases from 42% up to 70% of the specified data. The smallest extrusion nozzle diameter in connection with the smallest layer height provide the densest internal part structure, the lowest surface roughness and the best mechanical properties. Especially the ductility was controlled by the manufacturing parameters since the number of pores introduced in the internal part structure determine the number of crazes. Apart from ductility, even with low layer height but larger extrusion nozzle diameter, the resistance to failure of the material extrusion manufactured parts improves significantly and saves manufacturing time by a factor of 10.

## 1. Introduction

Additive manufacturing offers new perspectives towards rapid prototyping, rapid tooling, rapid manufacturing and rapid repair [1,2]. A variety of materials can be handled to realize an abundance of objects. A main technique to process thermoplastic polymers is 3D printing, for instance by fused filament fabrication (FFF). During the FFF process a thermoplastic polymer filament is melted, extruded and the strand is deposited on a build plate. The movement of the nozzle defines the strand deposition in the x and y directions of a plane. The three-dimensional workpiece is built up layer by layer in z direction [2]. The FFF process allows to quickly transfer a CAD (computer aided design) model into a real object. Due to tool-free production, highly structural freedom and low-costs are possible and the production of small series offers great flexibility [1,3]. Acrylonitrile butadiene styrene (ABS) is an amorphous low-cost mass-produced thermoplastic terpolymer commonly used in the automotive [4,5], health technology

[6] and plastic processing industry in a variety of ABS material grades [7,8].

In comparison to other established manufacturing processes in the plastic processing industry, e.g. injection molding, the layer-by-layer building up of the additive manufacturing FFF process leads to significant differences in the inner structure and surface topology of the parts. The structure which influences the quality of the manufactured component can be subdivided into three levels: micro, meso and macrostructure. The ABS grade respectively the manner of blend of the three monomeric units, i.e. a styrene / acrylonitrile copolymer matrix containing discrete butadiene-based elastomer particles, governs the microstructure inside the strands [9]. The orientation of the filament strands deposited in the workpiece as well as the welding quality and the size and distribution of existing voids between them can be regarded as the mesostructure or inner structure of the part. The external geometric shape of the additive manufactured part constitutes the macrostructure. In this study, we refer to the mesostructure of the parts.

\* Corresponding author.

E-mail address: [Daniela.Nickel@ba-sachsen.de](mailto:Daniela.Nickel@ba-sachsen.de) (D. Nickel).

The compositional anisotropy has a substantial impact on optic, haptic and mechanical properties [3,10]. Apart from investigations of optic and haptic appearance, the quality of polymer products is proved by testing mechanical properties, e.g. by tensile test [3]. In reference to establishing additive manufacturing in industrial applications, a deeper insight into the FFF process and its parameters is needed. The improvement, and moreover the repeatability of the mechanical properties is necessary to guarantee constant quality of the FFF polymer products and their applicability as engineering parts [11]. Furthermore, their surface topography and mesostructure play a decisive role in upgrading post-processing procedures such as electroplating [12].

The improvement of structural, optical, haptic and mechanical properties of FFF parts is conceivable by using different materials like ABS, PLA (polylactide) or PEEK (polyether ether ketone) [6,8,10,11,16,23,27] or by an optimization of the manufacturing process. Numerous research groups have strived to optimize the deposition of layers of fine threads of fluid thermoplastics. Commonly, a focus on five 3D printing parameters appears, i.e. layer height [11,13–20], distance [17,21] and orientation of the filament strands [10,14,16,17,21–25], infill density [14,19], orientation of the workpiece on the build plate [11,13–15,17,20–22,26]. Moreover, the 3D printing speed [9,13,20] and the temperature of the extrusion nozzle [14,23] are considered. Neuronal networks were applied for the decision on optimal printing parameters [17]. Moreover, for special applications the mechanical performance of ABS at 77 K became of interest and was correlated to the 3D printing settings layer thickness, raster pattern and infill [27]. Strain rate, impact strength and bending resistance were studied for two different ABS grades [28,29].

Nevertheless, compared to the benchmarks provided by the producers of the thermoplastics, mechanical properties of additive manufactured samples are still inferior. Exemplarily, printed ABS parts achieve at best two-thirds of the tensile strength (44 MPa) and around three-fourths of the elastic modulus (2300 MPa) specified in the data sheet for injection molded parts, respectively [15,30]. Additional issues are the temperature sensitivity of the mechanical properties of ABS [26], the fracture behavior under uneven stress distributions and under cumulative stress [31–33]. However, the variety of ABS material grades and their sensitivity to environmental conditions like humidity and temperature impedes the comparison of absolute values. However, with selected experiments on a defined ABS variety (Terluran GP 35), a comparison of 3D-printed specimens with different inner structures can be carried out.

So far, the build parameters of layer height and orientation of the strands have been considered to have the main influence on the enhancement of the mesostructure [34]. Using a heater block with the ability to simply exchange nozzles, the so-called Olsson block [35], facilitated the preparation of samples with different nozzles. This allows the nozzle diameters to be varied easily while other parameters remaining unchanged. Kuznetsov et al. [34] studied the mechanical behavior of PLA parts using a set of different nozzles and a range of layer heights for 3D printing. Samples with a defined wall thickness but no infill structure were investigated by three-point bending flexural tests; the mesostructure was analyzed by scanning electron microscopy (SEM). They found a decrease of strength when increasing the layer height, but an increase of strength with an increasing nozzle diameter. An investigation by Wang et al. [36] deals with the high-performance polymer PEEK stating that low layer heights and small nozzle diameters result in best mechanical performance and surface quality. Moreover, they evidenced the extrusion temperature as a very significant parameter.

A great number of studies that deal with the FFF process have examined the influence of the one-dimensional structural change (layer height) or the two-dimensional structural change (layer height and strand gap). However, there are only very few studies [34] of semi-crystalline thermoplastics and none of amorphous ones that deal with three-dimensional structural changes (layer height and nozzle diameter). The present work closes this knowledge gap and, at the same

time, provides a contribution to the question of how the damage mechanism of amorphous thermoplastics (ABS) is related to the production-related porosity of the FFF manufactured parts. Furthermore, the control of the component porosity and thus the control of selected mechanical properties from the tensile test by varying the three-dimensional structural change (layer height and nozzle diameter) is investigated. We strongly control the environmental conditions, especially humidity and temperature, within the whole production process to guarantee constant material quality and to ensure safe, reproducible processing from plastic granulate to additive manufactured product. A study of 5 × 15 tests was designed and conducted by varying nozzle diameter and layer height, but keeping constant other 3D printing parameters, namely strand orientation, fill density, shell thickness, build plate temperature and material flow. Mesostructure and surface topography are investigated by microscopic methods. Mechanical properties – elastic modulus, tensile strength and elongation at break – are determined by tensile tests. The aim is to create a deeper insight into the relation between porosity due to voids and welding quality between strands of additive manufactured ABS and its mechanical properties.

## 2. Expected porosity due to nozzle diameter and layer height variations

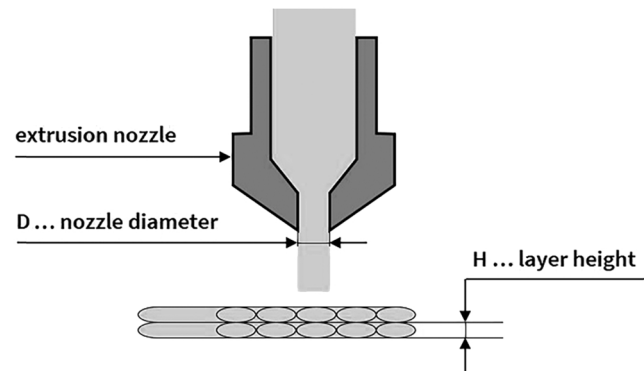
We used three different nozzles with diameters of 0.1 mm, 0.4 mm and 0.8 mm. The nozzle with a diameter of 0.4 mm represents the standard nozzle installed by the manufacturer. The layer height, respectively the thickness of the laid strands, is chosen to equal the nozzle diameter or is reduced to 0.1 mm.

Fig. 1 schematically shows the formation of the mesostructure which develops due to the remaining voids between the laid plastic strands. We suppose a major influence on the overall strand adhesion exerted by the number and size of the voids forming between the strands. Therefore, the porosity appears as a good measure describing the mesostructure of the printed material. Even though the real structure of the printed specimen will be examined by microscopic methods, we preliminary consider a theoretically expected porosity using the 3D printing parameters of nozzle diameter D and layer height H.

Porosity  $\varphi$  is the measure of the void fraction, i.e. the empty spaces in the material. It is defined as 1 minus the fraction of the volume of the material  $V_M$  over the total volume, i.e. the sum of the void volume  $V_V$  and the material volume  $V_M$  as given in Eq. (1). The formulas used are theoretical considerations. The approaches for our paper derive from various literature sources [10,34,37].

$$\varphi = 1 - \frac{V_M}{(V_V + V_M)} \quad (1)$$

Therefore, porosity is expected as a number between 0 and 1, or as a percentage between 0% and 100%. To consider the intended variation of



**Fig. 1.** Scheme of the influence of 3D printing parameters of nozzle diameter (D) and layer height (H) on the mesostructure of the workpiece.

the layer height, we define a ratio R between the layer height H and the nozzle diameter D according to Eq. (2).

$$R = \frac{H}{D} \quad (2)$$

In the first rough approach of spheres building up the material with corresponding cavities between, we set D = H and hence R = 1. Close packing of spheres (cubic or hexagonal) would result in a density of ~0.74 or a porosity  $\varphi$  of ~0.26, respectively. However, we assume the smallest regular packing, the single cubic sphere packing, as a preliminary isotropic model for the printed material. Using the nozzle diameter as the diameter of the spheres inside a cuboid, the porosity  $\varphi$  can be calculated by Eq. (3).

$$\varphi = 1 - \left( \frac{\frac{\pi}{6} \cdot D^3}{D^3} \right) = 1 - \frac{\pi}{6} = 0.4764 \quad (3)$$

3D printing of a body with length y not by depositing simple spheres but elongated plastic strands side by side makes the material anisotropic and transforms the empty spaces inside the sample into elongated voids. Thus we have to consider only the cross-section. The porosity can be calculated by Eq. (4).

$$\varphi = 1 - \left( \frac{\frac{\pi}{4} \cdot D^2 \cdot y}{D^2 \cdot y} \right) = 1 - \frac{\pi}{4} = 0.2146 \quad (4)$$

Reducing the layer height below the nozzle diameter results in strands with flattened cross-section circumscribed by a rectangle with sides  $D > H$  for further calculation. Once more, we consider the cross-section and calculate the resulting porosity by Eq. (5) using (2).

$$\varphi = 1 - \frac{\left( \frac{\pi}{4} \cdot H^2 \right) + H \cdot (D - H)}{D \cdot H} = \left( 1 - \frac{\pi}{4} \right) \cdot \frac{H}{D} = 0.2146 \cdot R \quad (5)$$

In our experiments, the ratio R between the layer height H and the nozzle diameter D varies between 1 and 0.125 thus reducing the expected porosity from around 20% to around 3% minimum.

It should be noticed that the estimation is based on strands with parallel deposition forming pores with cross sections assumed to be a rhomb or more accurate a circular arc quadrilateral. Actually, ~45°/+45° crisscross printed strands are studied, which undergo a larger deformation especially at the bottom of the threads. The connectivity of pores between parallel threads account for a higher total pore volume compared to the crisscross 3D printing where the porosity channels are shorter and dispersed. The observed pore cross sections rather resemble a triangle. Consequently, the actual porosity of the parts is supposed to be lower than estimated above.

### 3. Material and methods

#### 3.1. Material and tensile specimen geometry

The standardized and certified ABS granulate Terluran® GP-35 (INEOS Styrolution Europe GmbH, Frankfurt, Germany) is used in this study. The properties of the ABS Terluran® GP-35 thermoplastic material are summarized in the data sheet distributed by the producer [30]. The mechanical properties were determined on test specimens produced by injection molding according to ISO 527. There are no standardized tests for determining the mechanical properties of additive manufactured plastic components so far. Consequently, our mechanical tests are based on the above mentioned standard ISO 527 (DIN EN ISO 527) [38, 39] issued for conventionally manufactured plastic parts. The selected geometry including the dimensions of the test specimen match the specifications of type 1BA of the standard (Fig. 2). All specimens are oriented with the flat side facing the printer platform or build plate. The crosswise deposition of the strands with an angle of +/- 45° to the long

sides of the specimen (as shown in Fig. 2) was selected as this type of pattern is expected to provide the best mechanical properties for additive manufactured components [10]. Additive manufacturing considers workpieces as being comprised of two components: a wall structure also referred to as shell and a filling structure or infill. Both components influence the mechanical properties in different ways [40,41]. We decided to manufacture exclusively the infill using this structure as the test specimen. Therefore, we defined the wall thickness as being zero. The 3D printing parameters of the infill offer options which govern the mechanical properties of the test samples. Apart from some preliminary examinations, we focused on the +/- 45° crisscross deposition of the strands and a volume filling level of 100%.

For the evaluation of the mechanical properties, the specimens were subjected to a controlled tension until failure. Uniaxial tensile testing according to DIN EN ISO 527 [38,39] is most commonly used for obtaining the mechanical characteristics of isotropic materials. Additive manufactured parts always have an anisotropic material structure, nevertheless the tensile test is commonly applied to these samples. The following properties are determined from the received stress-elongation diagrams:

- Young's modulus, i.e. the modulus of elasticity in tension that quantifies the relationship between tensile stress and axial strain in the linear elastic region of the diagram according to Hooke's law.
- Yield strength, i.e. the upper limit of the stress at which the material deforms plastically.
- Elongation at break, i.e. the ratio between the changed length and the initial length after breakage of the test specimen, one of the quantities of ductility.

To carry out high-quality tests, the test specimens were stored in a constant climate cabinet at a temperature of 23 °C and a humidity of 5% for at least 24 h prior to the actual tensile test. The humidity was chosen to be that low because the ABS plastic is a hydrophilic material. The actual tensile tests were carried out under the following test conditions (Table 1).

#### 3.2. In-house process chain from granulate to specimen

We strived to control all steps from filament extrusion via filament storage to additive manufacturing. Defined handling under reproducible environmental conditions from granulate to printed specimens guarantees consistent material conditions within our study. Especially, the hygroscopic behavior of ABS demands a controlled low humidity to be integrated in the complete process chain (Fig. 3).

The process chain starts with drying the ABS granulate (Fig. 3a) in an AIRID polymer dryer (3devo, Utrecht, The Netherlands, Fig. 3b) directly after supply by the manufacturer. The corresponding setting parameters are summarized in Table 2. Drying is the most important process as the moisture content of the plastic granulate determines the quality of the filament.

The subsequent filament extrusion was performed by a desktop filament maker COMPOSER 450 (3devo, Utrecht, The Netherlands, Fig. 3c). The product is a spooled ABS filament (Fig. 3d). The production parameters for the extrusion of the plastic filaments are based on the standardized processing parameters of the machine manufacturer for the material ABS. The setting parameters are listed in Table 3.

Due to its hygroscopic behavior, the filament needs to be stored immediately after extrusion using the filament dryer APIUM F300 (Apium Additive Technologies GmbH, Karlsruhe, Germany, Fig. 3e). Filament storage started at 60 °C for 240 min before the material was kept at 40 °C until 3D printing. To avoid that the dry filament comes into contact with moisture again, a closed pipe connection was installed between the dryer and the production machine, an FFF 3D printer ULTIMAKER 3 (Ultimaker B.V., Utrecht, The Netherlands, Fig. 3f). The printer is equipped with a print head HARDCORE PRO-AA (3D Solex,

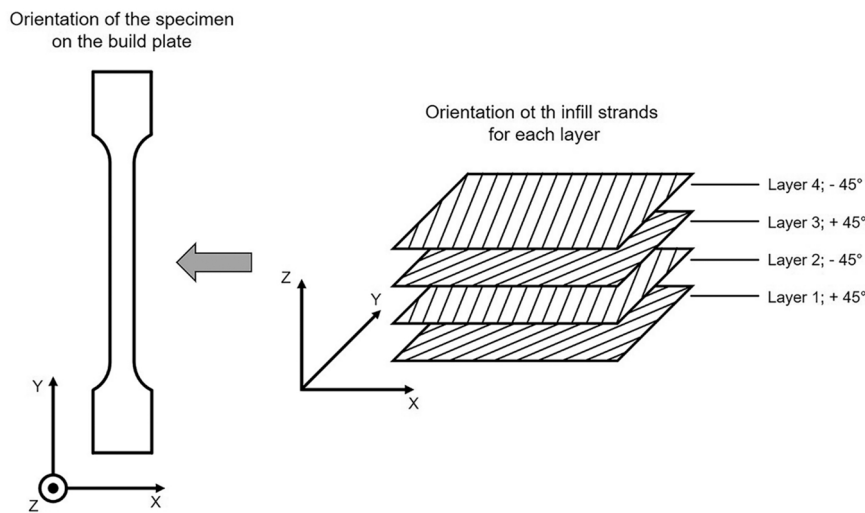


**Fig. 2.** Sketch of the tensile specimen according to ISO 527 1BA [26] showing the applied strand pattern.

**Table 1**  
Tensile test conditions.

Feature	Parameter
Room temperature	23 C
Humidity	50%
Elongation speed	1%/min
Extensometer sampling rate	1/100 s

**Table 2**  
Drying parameters for ABS Terluran® GP-35 granulate.

Feature	Parameter
Fan Speed Ratio	20%
Drying Temperature	80 °C
Drying Time	240 min
Mixer Speed	10 min <sup>-1</sup>

**Table 3**  
Extrusion parameters for ABS Terluran® GP-35 filament.

Feature	Parameter
Extrusion Speed	6.5 min <sup>-1</sup>
Fan Speed	85%
Filament Diameter	2.85 mm
Temperature Heater 1	225 °C
Temperature Heater 2	230 °C
Temperature Heater 3	235 °C
Temperature Heater 4	230 °C

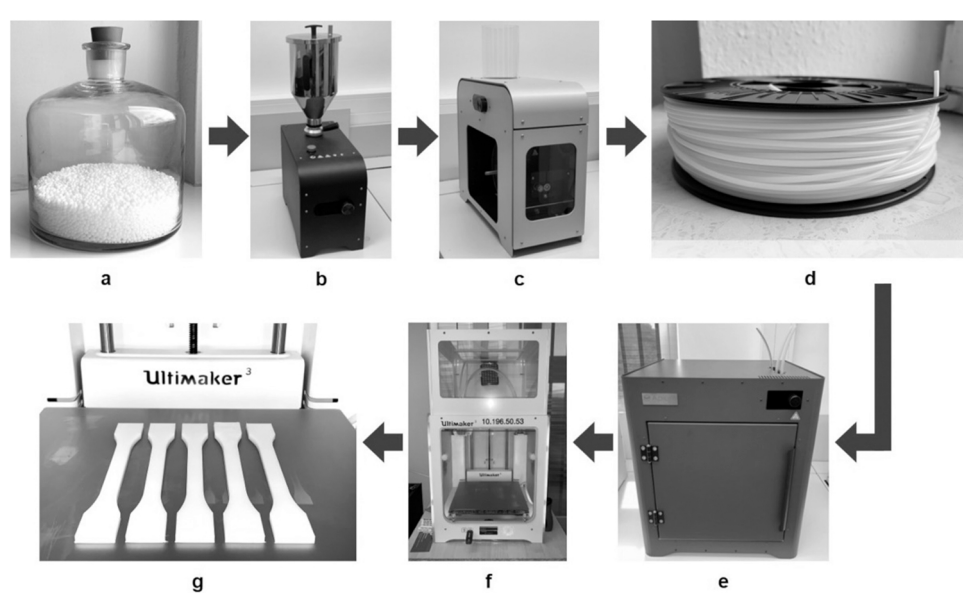


**Fig. 3.** In-house process chain, (a) ABS granulate, (b) granulate dryer, (c) filament extruder, (d) extruded filament, (e) filament dryer, (f) FFF printer, (g) printed tensile test specimens.

**Table 4**  
3D printing parameters for the test specimens.

Feature	Parameter				
Nozzle Diameter D [mm]	0.8	0.4	0.1	0.4	0.8
Layer Height H [mm]	0.1			0.4	0.8
Ratio R = H/D	0.125	0.25	1		
Wall Thickness	0				
Manufacturing Speed [mm/s]	30		10	30	
Material Flow	105%				
Volume Filling Level	100%				
Filling Direction	+/- 45°				
Manufacturing Temperature [°C]	250		270	250	
Build Plate Temperature [°C]	110				
Production Time [min]	10	23	227	5	1

individual parameter in order to find the best value. In the last step, the individual parameters with the best values were combined with each other and this combination results in the solution of the problem to be considered. The 3D printing parameters are listed in Table 4.

### 3.3. Experimental design and setup

As summarized in the first three lines of Table 4, the experimental design focuses on the mutual variation of the nozzle diameter and the layer height. At least 15 samples for each parameter configuration were examined for mechanical properties.

Prior to mechanical testing, the samples were stored under controlled homogeneous environmental conditions using the constant climate chamber BINDER KBF 115 (Binder GmbH, Tuttlingen, Germany). The samples were kept at a temperature of 25 °C and a relative humidity of 20% RH for 48 h.

Tensile tests were made using a material testing machine Z010 ProLine (ZwickRoell GmbH & Co. KG., Ulm, Germany). The elastic elongation was recorded by an extensometer digiclip (ZwickRoell GmbH & Co. KG., Ulm, Germany) with a gauge length of 25 mm. As stated above, the investigations were carried out according to DIN EN ISO 527 [38,39].

The surface topography was evaluated using a laser scanning microscope LEXT OLS5000 (MS) (Olympus Deutschland GmbH, Hamburg, Germany). The samples were aligned to measure the roughness of the top layer. The arithmetic mean roughness  $R_a$  was determined according to DIN 1302.

As an additional method for comparison, computed tomography scans (x-ray micro-CT scans) were used to evaluate the porosity of the samples. The system CT-ALPHA (PROCON X-Ray GmbH, Sarstedt, Germany) is equipped with a microfocus X ray tube XWT225SE (35 kV, 0.25 mA, focus diameter 10  $\mu\text{m}$ ) and a detector Varian Paxscan 2520. 1200 images were obtained by rotating the sample between 0° and 360° with an exposure time of 2 s, threefold image integration and 25x geometrical magnification. Data recording and 3D reconstruction of the volume data sets was effected using the software Volex (Fraunhofer IIS). The volume of the region of interest was a cuboid defined by 200 × 600 × 600 voxels (height × width × depth). The image resolution was 5.1  $\mu\text{m}$  per voxel. The data analysis and visualization software AVIZO 9.1.1 was used for the data processing of the CT scans.

Samples for optical microscopy were cut by an automated rotary microtome HistoCore AUTOCUT (Leica Biosystems Nussloch GmbH, Nussloch, Germany). The desired thickness of the thin sections was almost 50  $\mu\text{m}$ . Porosity was determined using the transmitted light microscope Axioscope 5 (Carl Zeiss Microscopy GmbH, Jena, Germany) in combination with the public domain image processing software ImageJ based on the microscopic images. Magnifications are given in the corresponding images by micron bars.

## 4. Results

### 4.1. Surface topography

Regarding surface topography, a distinction has to be made between different surfaces of a printed part. Obviously, the topography of the lateral walls or the shell will be influenced mostly by the layer height. The bottom side is mainly smoothed due to the contact with the heated built plate. Since we are interested in the properties of the infill only, we omitted the preparation of the shell. Therefore, the specimens are solely composed of the infill; and the top surface of the specimen has a topography which should be affected by the nozzle diameter and the strand height. In order to indicate the quality of the top surface, the most common roughness parameter  $R_a$ , i.e. the arithmetic average of the roughness profile, was studied by a laser scanning microscope. The roughness  $R_a$  is shown as a function of the nozzle diameter and the strand thickness in Fig. 4. The investigation of the surface roughness is a quick and easy way to obtain information about the porosity in the additive manufactured part. The lower the roughness of the surface, the lower is the roughness of each individual layer and thus the pore volume in the component decreases.

- The bottom side of the specimens, also referred to as adhesion side, exhibits the lowest surface roughness  $R_a = 0.5 \mu\text{m}$  due to its contact with the heated support.
- The top surface of the printed parts shows significant differences in roughness. Low roughness values of  $R_a < 5 \mu\text{m}$  were determined as long as the layer height is low (0.1 mm) and nearly independent of the nozzle diameter ( $R = 0.125$ ,  $R = 0.25$  and  $R = 1$  for 0.1 mm nozzle).
- The surface roughness increases by a factor of 10 when the largest layer height ( $H = 0.8$ ) and the largest nozzle diameter ( $D = 0.8 \text{ mm}$ ) are applied.

CT scans of the samples (Fig. 5) confirm not merely the layer height but even more the nozzle diameter influence on the surface roughness. This will be represented as a good example in the comparison between Fig. 5a and 5d. A medium nozzle diameter and the lowest strand height occur as an optimum parameter combination providing a rather low roughness without expansively boosting the 3D printing time (Fig. 5b), although the smallest nozzle diameter creates the densest and smoothest surface (Fig. 5c) whereas a large nozzle diameter results in a rather open and rough surface (Fig. 5d).

### 4.2. Features of thin sections in optical microscopy

Features of the mesostructure of FFF printed parts are inspected by means of optical microscopy on thin slides. The cross-sections clearly display individual strands that constitute the part as well as voids between them. In a preliminary examination, three thin samples, each with different strand deposition directions, were sliced. Following, 3D printing routes were applied: crosswise 3D printing in the x-y plane of the tensile specimen with +/- 45° rotation relative to the symmetry axes, the crosswise 3D printing with 0°/90° referring to the symmetry axis and only unidirectional.

Fig. 6a reveals that the strand deposition of +/- 45° provides a relatively dense mesostructure. The other two 3D printing alternatives 0°/90° (Fig. 6b) and unidirectional (Fig. 6c), respectively, result in larger cavities between the strands, which weaken the printed structure.

Ramezani Dana et al. [10] stated that the strand deposition pattern +/- 45° is the variant delivering tensile specimen with mechanical properties closest to that of injection molding components. Since our preliminary studies confirmed that finding, all further tests were carried out using the +/- 45° 3D printing pattern. The denser the mesostructure and the fewer the defects noticeable in the component, the better the mechanical properties of the additive manufactured component are

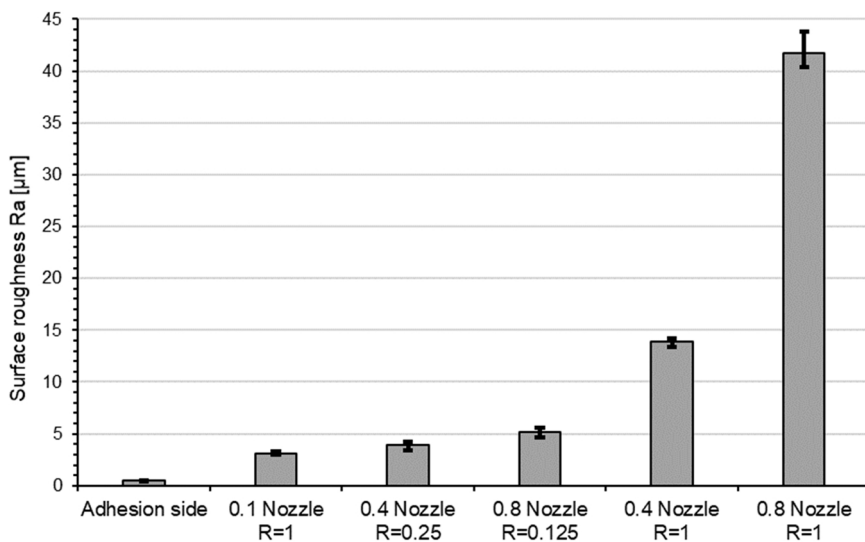


Fig. 4. Surface roughness  $R_a$  as a function of the different nozzle diameters and the H/D ratio.

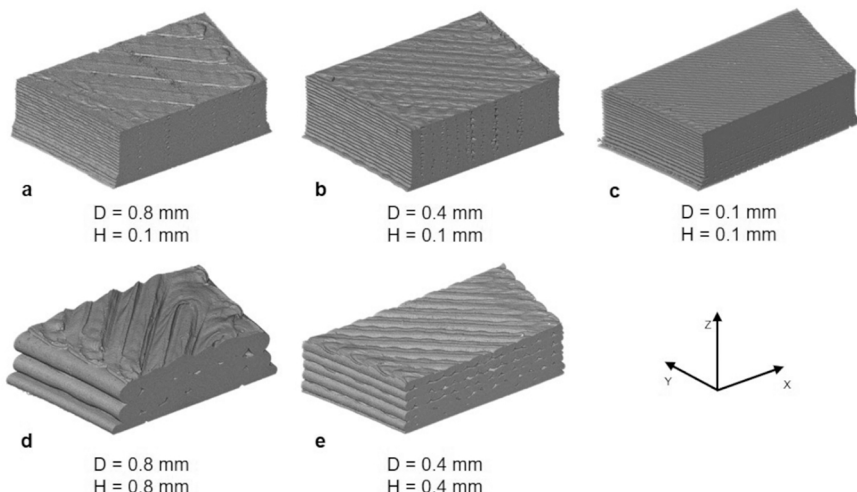


Fig. 5. CT scans showing the surface and the cross-section of the samples; the complete width (x) and height (z) of the test specimens and 5 mm in y direction are shown.

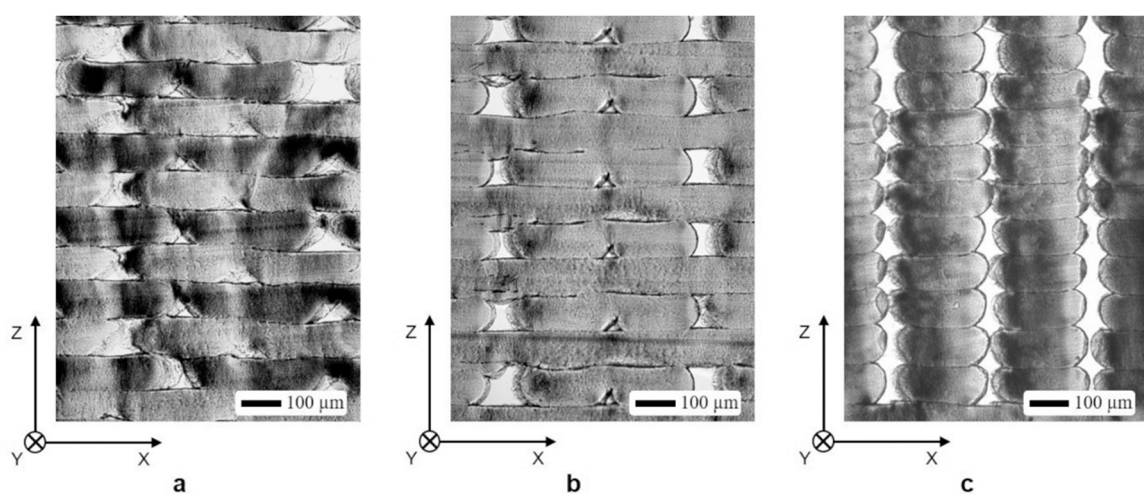


Fig. 6. Transmitted light microscopy of specimen with different strand orientation in the x-y plane: +/- 45° (a), 0°/90° (b) and 0° (c). The z axis defines the direction in which the tensile specimen is built up layer by layer, cut direction is from right to left in x-z plane.

expected to be.

#### 4.3. Porosity

The influence of the nozzle diameter and the layer height on the mesostructure of the FFF samples is demonstrated in Fig. 7. Transmitted light microscopic images show thin slices of the samples sectioned in the x-z plane of the specimen. All samples were taken from the middle area of the corresponding test specimen. The FFF samples shown in the upper row were printed with the same layer height  $H = 0.1$  mm and a decreasing nozzle diameter from  $D = 0.8$  mm (Fig. 7a) to  $D = 0.1$  mm (Fig. 7c). The micrographs in the lower row represent the nozzle diameters with equivalent larger layer heights matching the ratio  $R = 1$  (Fig. 7d and e).

Obviously, the low layer height in the 3D printing protocol results in a low strand thickness and provides an overall denser microstructure with lower porosity regardless of the nozzle diameter. Pores of almost triangular cross-sections are formed in the contact zones of the strands. Their size reduces with decreasing layer height and decreasing nozzle diameter. Overall, the shape of the strand cross-section is flattened compared to the pore model in chapter 2. Especially in the delicately printed sample with  $H = 0.1$  mm and  $D = 0.1$  mm, the pores show a remarkable coalescence. These features influence the actual porosity of the printed material and lower the actual values compared to the theoretically expected porosity. The porosity was quantified with the aid of the image analysis program ImageJ applied to the microscopic images

of thin sections. For this purpose, the micrographs were converted into grayscale images. A limit was set to differentiate between the ABS material and the pores between. The area of the pores in relation to the total area  $A_I$  (6) of the image gives the porosity provided uniform distribution of the pores.

$$A_I = 1081.3 \mu\text{m} \cdot 811 \mu\text{m} = 876934.3 \mu\text{m}^2 \quad (6)$$

To verify the microscopic results, CT scans were evaluated. Fig. 8 shows two different representations of the samples derived from the CT data, the printed workpiece and the pore network. Fig. 8a1–8e1 represent a unit cuboid of the printed samples showing their 3D view. In either case of similar size and taken from the center of the scanned specimen, the unit cuboid of  $200 \times 600 \times 600$  voxels with a resolution of  $5.1 \mu\text{m}$  per voxel was the basis of the porosity evaluation carried out by the software AVISIO 9.1.1. The reconstructed pore networks are shown in Fig. 8a2–8e2. Thus, the volume of the pore network could be determined and put in relation to the volume of the unit cuboid for the porosity evaluation. Table 5 summarizes the various results derived from the consideration under paragraph 2 (column 2), from image analysis (column 3), evaluated from the measured Young's Modulus, see also "Mechanical properties" (column 4) and from X ray CT scans (column 5). The results show some discrepancies. For  $R = 1$ , the theoretically estimated porosity is remarkably too high which results from the deformed strands in crisscross 3D printing. Thus, the pore channels are shorter, their opening size is smaller, and the total porosity is lower as

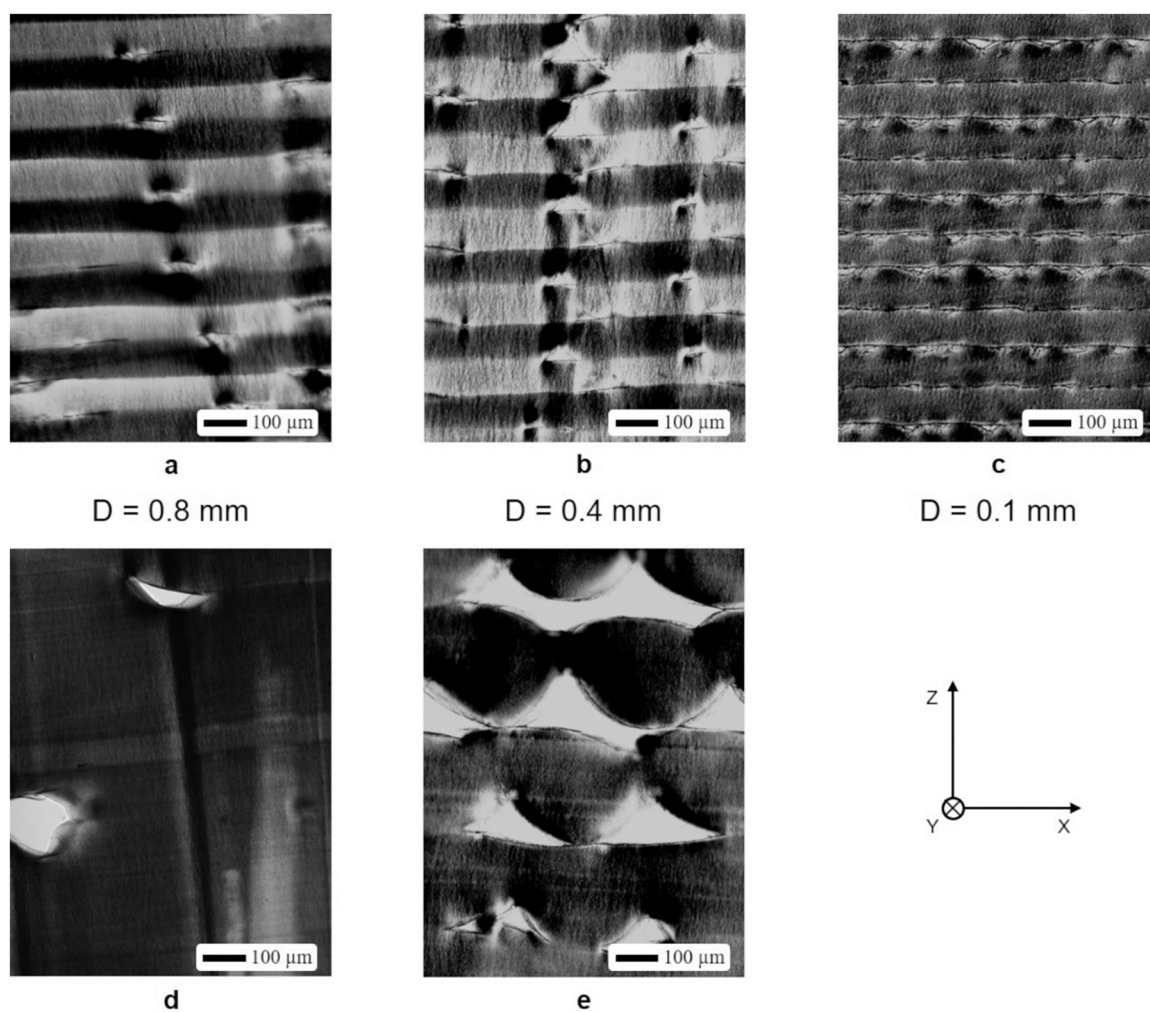


**Fig. 7.** Thin sections of specimens, (a)–(c) printed with layer height of 0.1 mm, (d) with 0.8 mm layer height and (e) with 0.4 mm layer height, the nozzle diameters are given in the figure, the micrometer bar is indicated in each individual micrograph.

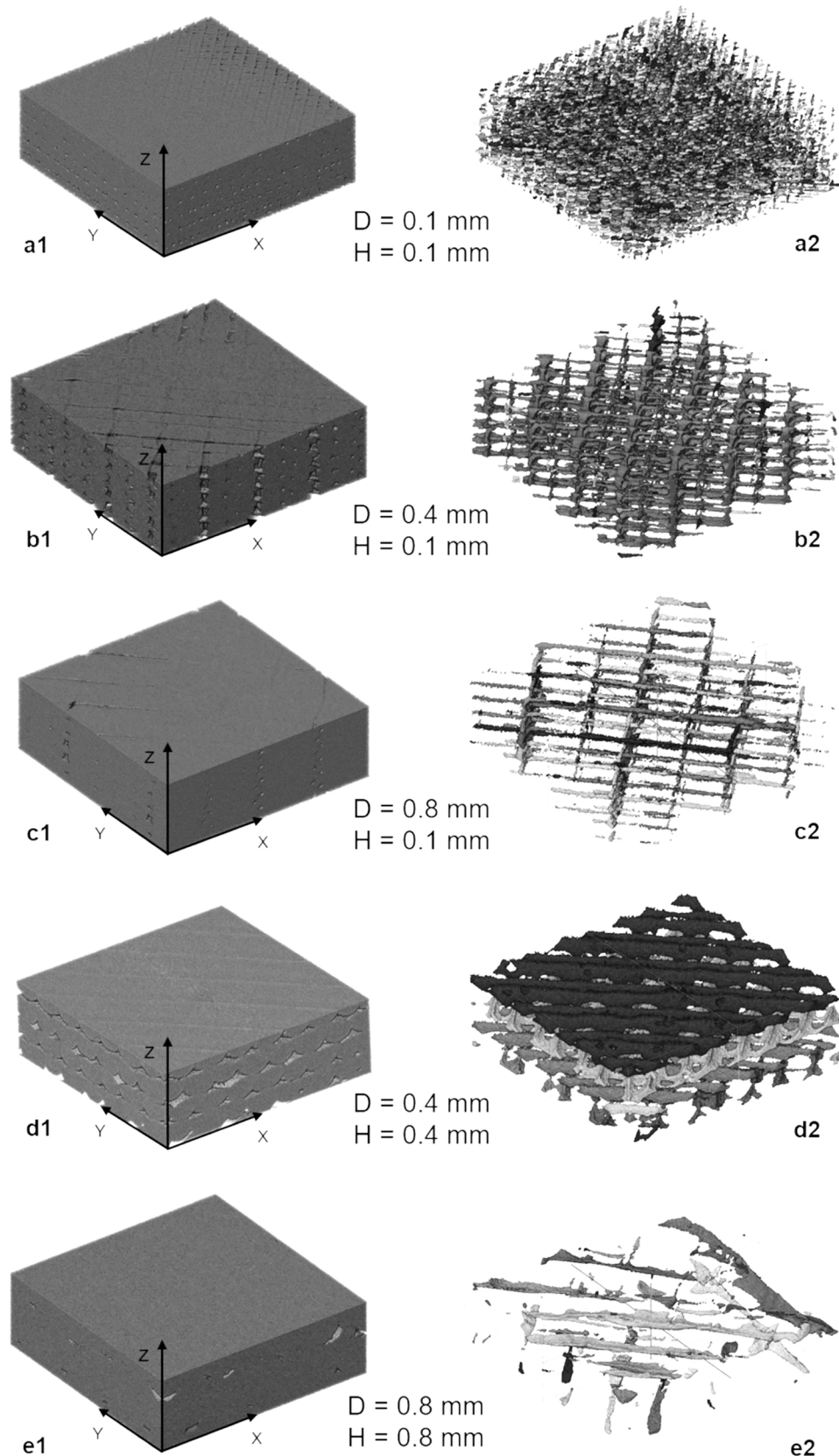


**Fig. 8.** CT scans of a unit volume in the center of the 5 specimens (a1-e1) and representations of the pore network inside the unit volume of the 5 specimens (a2 - e2).

**Table 5**

Porosity evaluated by calculation, image analysis, according to the Young's modulus and X ray computed tomography.

Ratio R, Diameter D	Theoretical porosity	Image analysis	Youngs modulus	X ray CT analysis
H = 0.1 mm D = 0.1 mm R = 1	[21.5%]	0.5%	0.8%	2.9%
H = 0.1 mm D = 0.4 mm R = 0.25	5.4%	3.1%	3.4%	5.9%
H = 0.1 mm D = 0.8 mm R = 0.125	2.7%	1.9%	2.8%	1.3%
H = 0.4 mm D = 0.4 mm R = 1	21.5%	13.5%	10.1%	9.5%
H = 0.8 mm D = 0.8 mm R = 1	21.5%	[5%]	10.6%	[1.7%]

discussed in chapter 2. In the case of the 0.8 mm/0.8 mm sample, the corresponding image and CT analysis do not meet statistical requirements. However, it must be taken into account that only a small number of voids were considered. There seems to exist a further effect, a kind of size effect/volume effect where no larger voids arise due to the larger volume of strand material. The second overlapping effect results from the less uniform welding between these strands. We assume an uneven heating which is seen as the reason for the poorer mechanical properties.

These considerations show the difficulties involved in an accurate estimation of the porosity. Nevertheless, the results can be summarized as follows:

- The coarsest mesostructure with the highest porosity is fabricated when using large layer heights.
- The densest mesostructure with the lowest porosity was found when using the lowest values of nozzle diameter and layer height.
- Regardless of the nozzle diameter, low layer heights result in low strand thickness and low porosity.
- The mesostructure and the number of pores in an additive manufactured product can be influenced and controlled by the manufacturing parameters of layer height and nozzle diameter.
- As the layer height is reduced, the number of pores in the z direction (construction direction) is increased, see Fig. 8d2 with a large layer height and Fig. 8b2 with a small layer height.

- By reducing the nozzle diameter, the number of pores within a layer or plane can now be increased, see Fig. 8a2–8c2. However, the total pore volume decreases in the complete component.

#### 4.4. Mechanical properties

The stress-strain diagram in Fig. 9 represents five experiments for each nozzle diameter / layer height combination. The total number of tests for each parameter combination is 15, however, the number of curves is limited for clarity. As expected from standard [38], the curves present a quasi-linear elastic portion of up to 2% strain and a yielding deformation on a tension level until specimen failure. The resisting stress is nearly constant with increasing deformation after having reached its peak. The tested specimens exhibit a high repeatability in the elastic region, but a striking variability of strain until failure. The superiority of the combination D = 0.1 mm and H = 0.1 mm is remarkable. A detailed analysis of the Young's modulus, yield strength and elongation at break follows in the next paragraphs.

##### 4.4.1. Crazing

The thermoplastic ABS is a blend of two phases, a soft and a brittle one. The glass-like polystyrene/acrylonitrile (SAN) matrix contains rubber-like polybutadiene (BP) particles which serve as centers for stress concentration. Inelastic deformation of the terpolymer begins with the cavitation of the particles. Once the brittle-ductile transformation is initiated, yielding of the matrix occurs. The deformation energy is consumed by shear banding commonly observed under compression or stress whitening or crazing observed under tension, respectively. Crazing as the main damage mechanism in vitreous and amorphous thermoplastic materials such as ABS is connected with an increase in volume since entangled chains are lost through disentanglement or scission thus producing craze fibrils [7,45]. Under tensile load, deformation occurs by formation of pseudo-cracks containing highly stretched polymer material, i.e. craze fibrils which connect the crack flanks. Thus, the fibrils allow for stretching while transferring the load. Crazes can be identified very well in the glass-like and partially transparent thermoplastic ABS, as they always appear perpendicular to the main tensile stress direction as white regions because of light scattering on the crazes. The multitude of “bands” formed at right angles to the direction of the applied stress were found to contain birefringent polymer of lower average refractive index than the surrounding bulk polymer [46].

Using macrophotography, the craze patterns of selected specimens after tensile testing and fracture were recorded. The specimen (Fig. 10a) represents a 3D printed tensile specimen before the tensile test was

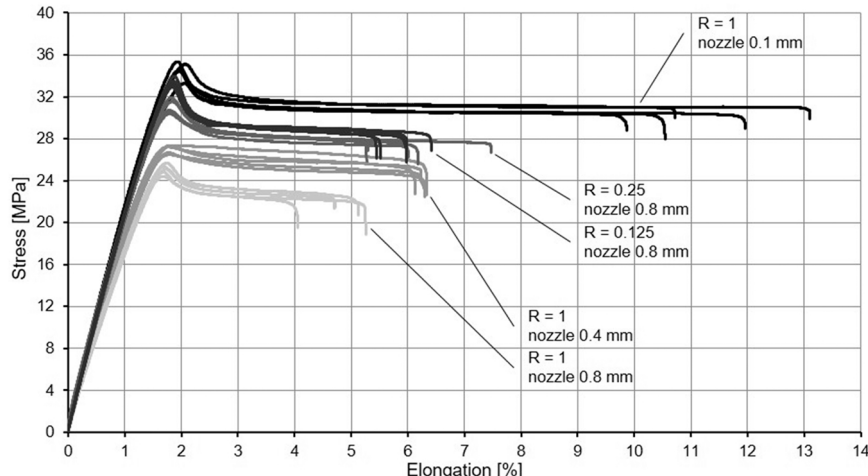


Fig. 9. Stress-elongation diagram of the samples with different 3D printing parameters showing the strength phase and the ductility phase typical for ABS.

carried out and is comparable with the specimen in Fig. 10c after testing. The structure shown in this illustration results from the additive manufacturing process FFF and reproduces the pattern of the strands deposited in layers. The specimens with different parameter combinations (Fig. 10b–f) illustrate the influence of the 3D printing parameters on the craze patterns. Obviously, crazes offer an excellent opportunity to visualize the deformation. The remarkably different craze patterns cannot be explained only by cavitation of rubber particles as the printed material has a constant composition ensured by the in-house manufacturing line. Comparing the 3D printing parameter dependent porosity of the specimen with the developing crazing suggests that the manufacturing-related voids are additional centers of stress concentration and therefore the origin of the different craze patterns. A proof that the resulting notches form the starting points of the crazes is illustrated in Fig. 10.

The photos show microscopic images of thin sections of an additive manufactured sample before (Fig. 11a) and after (Fig. 11b) the specimen was subjected to tensile load. The voids (1) and the boundaries between the deposited strands (2) can be easily recognized in transmitted light. Additionally, Fig. 11b reveals that many bright areas (3) have emerged. These areas represent the crazes that were created by the application of tensile stress. It shows that the voids are the starting point of the crazes and that they spread out in the direction of the boundaries between the strands. Consequently, the number of crazes depends on the number and size of the voids in the mesostructure of the additive manufactured components.

#### 4.4.2. Young' modulus $E_t$

Fig. 12 shows the modulus of elasticity for different nozzle diameters D and layer heights H. Since the elastic elongation range in plastics is very small, the modulus of elasticity was calculated between an elongation of 0.05% and 0.25%. The formula for calculating the modulus of elasticity  $E_t$  (7) and the corresponding elongation values derive from the standard [38,39]

$$E_t = \frac{\sigma_{0.25\%} - \sigma_{0.05\%}}{0.0025 - 0.0005} \quad (7)$$

1. Young's modulus  $E_t$  can be grouped into two categories.
2. The lowest results are obtained from the parameter combination large nozzle diameter / high layer height. By reducing the layer height, the Young's modulus  $E_t$  increases, which is confirmed by literature [34,36].

3. Nevertheless, the highest Young's modulus, fairly similar to the value given in the data sheet of the material ABS Terluran® GP-35, is reached when using the lowest nozzle diameter and the lowest layer height.

#### 4.4.3. Yield tensile strength $\sigma_m$

1. Significant differences in the maximum tensile strength  $\sigma_m$  are observed (Fig. 13).
2. Two groups of data can be stated: large nozzle diameters and high layer heights result in low yield tensile strength. Reducing the layer height to 0.1 mm regardless of the nozzle diameter results in almost similar, relatively high values of yield tensile strength.
3. According to the data sheet of injection molded ABS, with the yield tensile strength being 44 MPa [30], the best result is reached with the combination of lowest nozzle diameter and the lowest layer height which averages 75% of this value.

#### 4.4.4. Elongation at break $\varepsilon_B$

1. Significant differences in the ductility of the specimens are observed (Fig. 14).
2. For the ratio  $R = 1$  we observe a rising elongation at break with decreasing nozzle diameter.
3. Using a low layer height but a large nozzle diameter does not remarkably improve the elongation at break.
4. Using the combination of smallest nozzle diameter 0.1 mm / lowest layer height 0.1 mm, the elongation at break repeatedly compares to 70% of the specification in the data sheet. Commonly, the elongation at break is increased by a mean factor of 2.

## 5. Discussion

Comparing the photographs in Fig. 6, striking contrasts inside the strands can be seen. This effect becomes particularly clear when examining the sample with the strand orientation of +/- 45° (Fig. 6a). Alternating bright and dark horizontal stripes are evident which can be understood as an optical effect of the printed plastic threads in transmitted light. The amorphous and partially transparent polymer ABS is exposed to strong shear during extrusion in the FFF process. The occurring shear thinning leads to a partial disentanglement and alignment of the molecular chains along the direction of the shear. The opaque ABS variants are obtained by matching the refractive index of

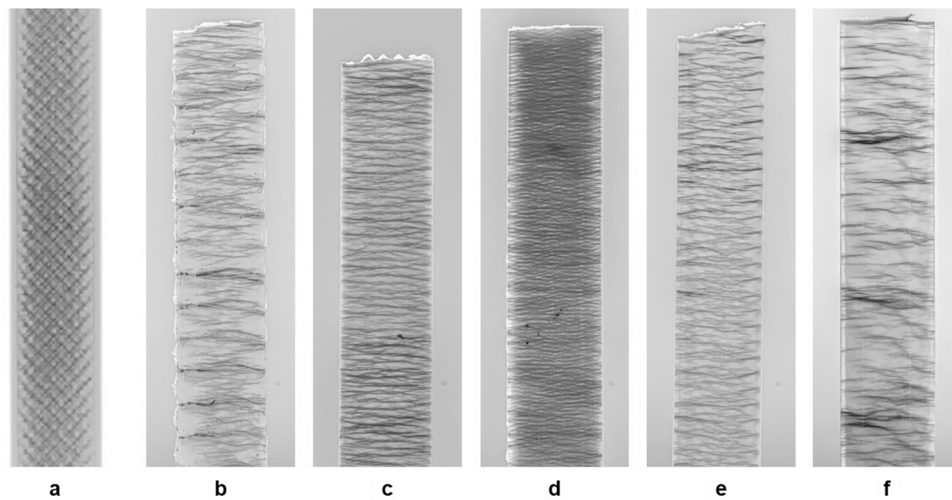


**Fig. 10.** Macroscopic recording of craze patterns of tensile test specimens near the fracture surface. The illustration (a) shows, for example, an untested specimen with the specification D = 0.4 mm / H = 0.1 mm. The specimens have a width of 5 mm. (b) D= 0.8 mm / H= 0.1 mm, (c) D= 0.4 mm / H= 0.1 mm, (d) D= 0.1 mm / H= 0.1 mm, (e) D= 0.4 mm / H= 0.4 mm, (f) D= 0.8 mm / H= 0.8 mm.

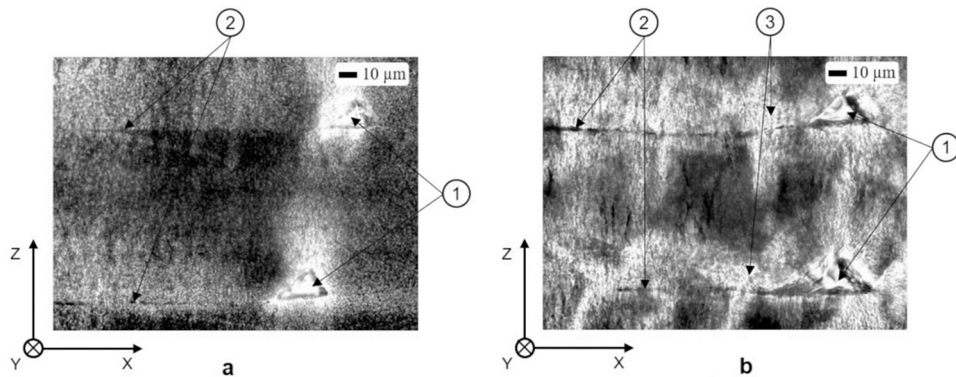


**Fig. 11.** Transmitted light microscope images of an additive manufactured tensile specimen in two different states: (A) unloaded and (B) after loading before failure. The following features are marked: (1) triangular voids between strands, (2) boundaries between three strands and (3) examples of areas of crazing.

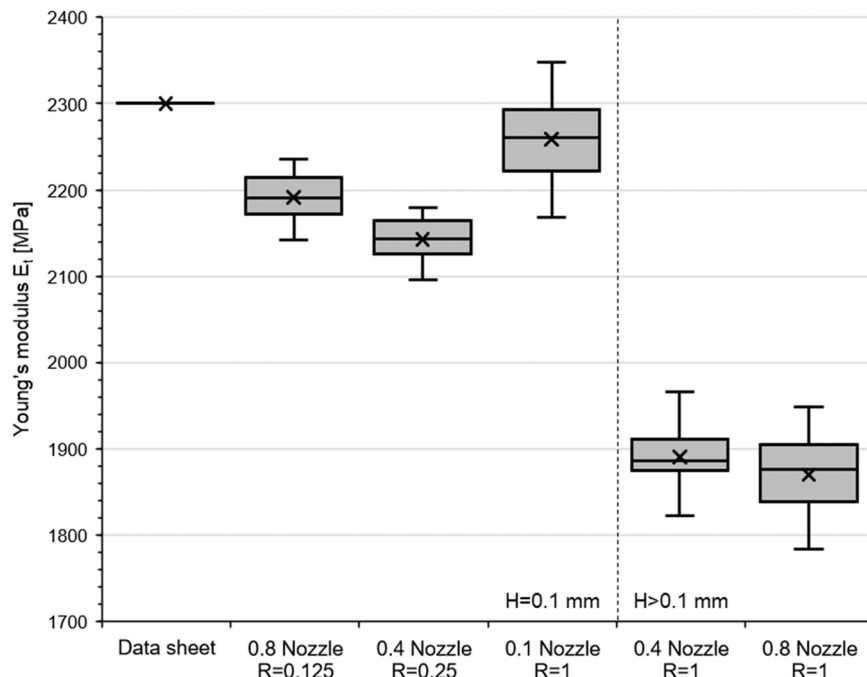


**Fig. 12.** Young's modulus for different nozzle diameters and ratios R.

the hard phase to that of the polybutadiene soft phase by copolymerization with methyl methacrylate. Shear stress disturbs the original isotropy inside the terpolymer. Hence, phase separation causes the anisotropy of optical properties, i.e. refraction, polarization and birefringence [47]. This effect dominates when the strand orientation is  $+/-45^\circ$  with respect to the slicing plane. Thin sections with perpendicular sliced threads of  $0^\circ/90^\circ$  crosswise or unidirectional print direction do not show this special contrast effect (Fig. 6b, c). Certainly, Fig. 6c displays also bright and dark contrasts, which, however, have a different origin. Cutting the samples by means of the sharp microtome knife perpendicular to the unidirectional arranged strands deforms the relatively ductile plastic material. As a result of the low welding, which leads to a low adherence between the poorly interconnected strands, the cut starts at the desired low thickness (left strand side in Fig. 6c). However, the loosened elastic strands do not provide sufficient counter bearing. The cut becomes thinner, which is reflected in the increasing lighter appearance (right strand side in Fig. 6c).

Like numerous researchers, we found that FFF printed materials show remarkable differences in mechanical properties when compared with the properties of injection molded parts. Through our

investigations we have determined various effects that are related to the mesostructure of the printed parts and its modification by changing the 3D printing parameters. The FFF parts qualitatively show the typical behavior of thermoplastic ABS in the tensile test [38]. The stress-strain curve can be divided into two regions (Fig. 9). The first "strength region" provides information about the stiffness and strength of the manufactured part. Especially the linear elastic part of this phase with the Young's modulus as its slope is significantly influenced by the porosity. Consequently, the highest Young's modulus, fairly similar to the value given in the data sheet of injection molded ABS Terluran® GP-35, is reached when using the lowest nozzle diameter / layer height combination which provides a mesostructure with very low porosity, precisely a low total pore volume.

The threshold between the "strength region" and the "ductility region" is the yield tensile strength which is not only influenced by the porosity of the mesostructure. Principally, it depends on the maintenance of cohesion between the individually deposited strands both in the plane and in the z direction. Injection molded parts occasionally include individual similar inconsistencies typically known as weld lines. They occur when polymer chains disentangle across the flow-front

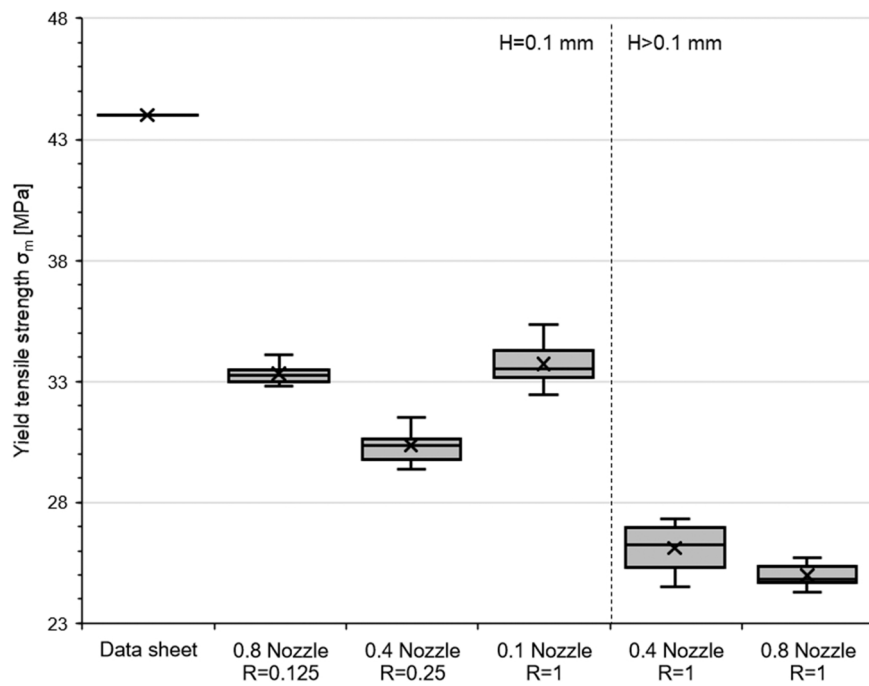


Fig. 13. Yield strengths  $\sigma_m$  for different nozzle diameters and ratios R.

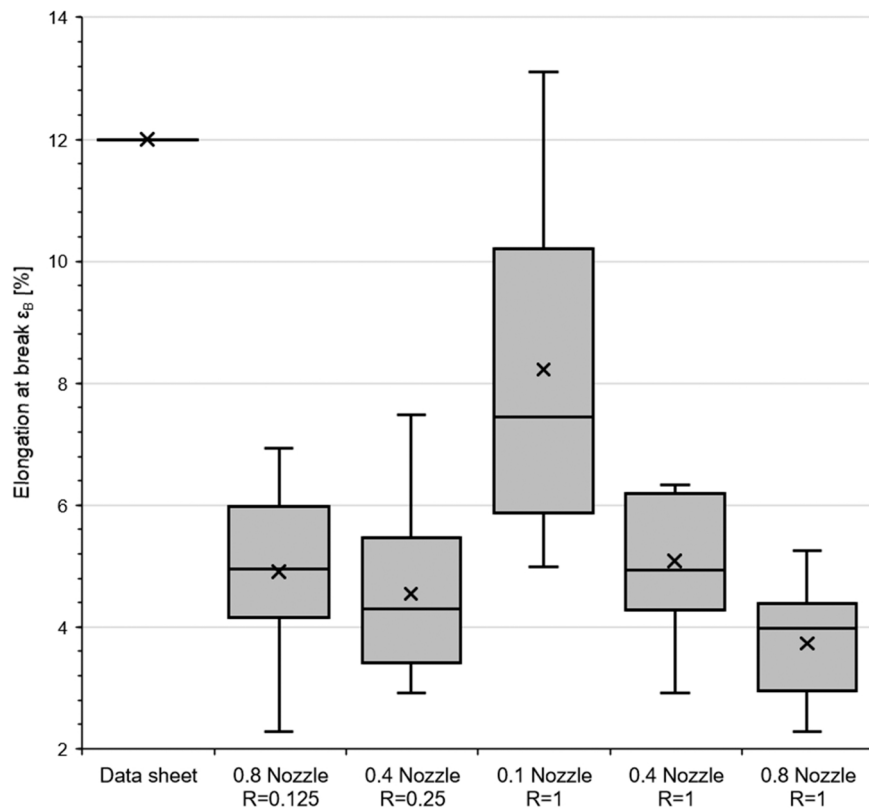


Fig. 14. Elongation at break  $\epsilon_B$  for different nozzle diameters and ratios R.

boundaries of the material. Unfortunately, the benzene rings in the ABS random structure, which are responsible for higher viscosity, reduced shrink rate and increased strength, are also vulnerable to disentanglement. Thus, the main reason for weld-line weakness in injection molded parts is the lack of polymer chain entanglement across the junction of the two flow fronts [48]. Regarding FFF printed parts, the quality of the

numerous welds between the strands determines the mechanical properties. The polymers become highly stretched and aligned during the deposition of the strands comprising extrusion, a 90-degree bend and the alteration from circular to elliptical cross-sections. The exerted shear causes disentanglement. Entanglement recovery is required for a good welding between the most recently extruded polymer strand and the

previously printed thread. A model of non-isothermal polymer relaxation, entanglement recovery, and diffusion processes was proposed by McIlroy and Olmsted [49] and reveals that disentanglement in the nozzle combined with the delay in re-entanglement due to the relaxation of the laid thread is the key mechanism responsible for a reduced mechanical strength in the weld regions. Thus, the quality of printed FFF parts depends on successful re-entanglement of the polymer melt across the layer-layer interfaces. A rising injection velocity, rising 3D printing velocity, and rising temperature of the 3D printing support [50] improve the re-entanglement and interdiffusion.

However, these parameters were kept constant and thus did not affect the variation of weld strength in this study. Regardless of the nozzle diameter, we always found relatively high values of yield tensile strength when the layer height was low. This seems to be related to the positive influence of the high shear stress which also causes high viscosity of the melt and lowers the total pore volume in the mesostructure of the printed part. Otherwise, the performance of the largest nozzle / low layer height material could be improved compared to the medium nozzle / low layer height material as the total contact surface area is larger and the number of welds is lower.

The Young's modulus  $E_t$  is a measure for the tensile stiffness of the printed material. Roughly, it accounts for how much the specimen extends under tension regardless of the empty spaces in between as long as the porosity is low [10]. The empirical formula [10] for roughly predicting  $E_t$  (8) of the tensile specimen according to its known porosity  $\varphi$  is

$$E_t = E_D \cdot e^{-b \cdot \varphi} \quad (8)$$

Using the first two terms of the Taylor expansion (9) and the constants according to [51].

$$E_t = E_D \cdot (1 - 1.9 \cdot \varphi + 0.9 \cdot \varphi^2) \quad (9)$$

with  $E_D$  being the Young's modulus given in the data sheet [30] and  $E_t$  the Young's modulus measured by tension tests, the porosity  $\varphi$  of the specimen can be estimated. The results are presented in Table 5. These results show very clearly that the modulus of elasticity of the 3D printed specimens depends on the porosity. The porosity of the 3D printed components is possible due to the three-dimensional structural changes when using the FFF process. Thus, not only the layer height but above all the nozzle diameter has a major influence on the porosity and thus also on the modulus of elasticity of the additive manufactured parts. This means that the smaller the additive structures (layer height and nozzle diameter), the greater is the modulus of elasticity.

The decrease of the yield tensile strength compared with the value from the data sheet is correlated with inherent pores caused by the FFF-process. Once the yield tensile strength  $\sigma_m$  is exceeded, the second region of the stress-strain-curve is the ductility phase which provides information about the resistance to failure of the component. The main damage mechanism in ABS is crazing. During craze growth, the cavities become increasingly larger and the fibrils form. When the fibrils have reached their maximum elongation and the crack flanks are no longer connected, crack formation occurs and the component fails. Crazing as a kind of plastic flow in polymers is the source of stress relief or toughness. Crazing requires a large number of discontinuities in the material, which are also sources of subsequent ultimate fracture. Consequently, it is not surprising that the elongation at break shows a broad variation. Printed parts using the combination of the smallest nozzle and the lowest layer height repeatedly reached an elongation at break which compares to 70% of the specification in the data sheet.

Apart from the broad variation, the elongation at break depends on the mesostructure of the part. Since craze initiation begins in areas of stress concentration that arise from phase differences or voids in the material, the 3D printing protocol controls the number of pores in the FFF part. The formation of voids additionally to the constant quantity of polybutadiene particles in the ABS base material makes it comprehensible that the elongation at break is occasionally higher than the

reference for injection molded parts. In turn, the mesostructure of FFF parts can be controlled by the production parameters of layer height and nozzle diameter. Thus, the number of crazes can be influenced by influencing the porosity. It should be noted that in this regard the number of pores is the decisive factor for the ductility of printed ABS parts. According to Fig. 14, specimens exhibited a more brittle behavior than the injection molded material. This behavior is due to the porosity and the resulting crazing. The elongation at break in the data sheet [30] is based on injection molded parts that are not supposed to have any porosity. The additive manufactured test specimens with the FFF process, on the other hand, always have a production-related porosity. The lower the porosity in the specimen, the greater is the elongation and thus the ductility. The results for this study are therefore acceptable and were as expected. The spread of the elongation values for the specimen specification  $R = 1$  with the diameter  $D = 0.1$  mm is very large compared to the other specifications. The reason for this is the different training of crazing over the test length. Crazing is a typical damage mechanism in amorphous thermoplastics and always occurs at imperfections [7,45]. An increasing number of pores with minimal volume results in an increasing number of micro-expansions in the form of these crazes and thus an increasing macro-expansion in the component. If the crazing develops evenly over the entire test length, high macro-elongations result. In the case of local crazing, on the other hand, the macro-stretching is low, as shown in Fig. 14.

The tensile tests are sufficient for this work since it aims to show the effect of controlling the porosity of additive manufactured components on the resulting mechanical properties. The mechanical properties are increases continuously when the porosity of the components decreases (Fig. 9). In addition, the pore size and the number of pores play a decisive role. The best mechanical properties are achieved when the total pore volume is minimal, while the number of pores is maximized. The pores in the FFF made of ABS material are the starting point for the damage mechanism of crazing. The higher the number of crazing, the better is the ductility of the additive manufactured parts. Further studies should include the formation of micro shear bands, which are known as featureless deformation zones accompanying the crazes provided that the pores are below 1 μm in diameter in ABS polymers [52]. Such micro shear bands can function as craze stopping mechanism and shift the limit to ultimate failure.

## 6. Conclusions

Tensile specimens were fabricated by Fused Filament Fabrication of acrylonitrile butadiene styrene (ABS Terluran GP 35) using an in-house process chain from granulate to product. Thus, all parameters and conditions were kept reliably constant, except for the variation of the parameters extrusion nozzle diameter and layer height. Based on the results of this study, the following conclusions are drawn:

- The FFF parts reveal a wide variation in pore size and porosity. The lowest porosity is connected with the lowest pore size but the highest pore number.
- Especially a low strand thickness obtained by the lowest layer height improves the mesostructure with minuscule pores, a porosity below 5% and a surface roughness Ra below 5 μm. The dense mesostructure is mirrored by a Young's modulus, reaching more than 93% compared to that of injection molded ABS.
- Regardless of the nozzle diameter, the yield strength rises from 55% to 75% compared to the specification for injection molded ABS as long as the strand height is low. However, the elongation at break stays low for the most nozzle/layer combinations.
- The yield strength was satisfactorily improved when using larger nozzle diameters but keeping the layer height low, which also keeps manufacturing costs low.
- Only by using the combination smallest nozzle diameter / smallest layer height, the densest mesostructure, the lowest surface roughness

- and the best mechanical properties were obtained. However, the fabrication time rose by a factor of 10. 70% of the elongation at break specified for injection molded ABS was achieved on average.
- The ductility of the parts is influenced by the number of crazes which are controlled by the development of the pores due to the manufacturing parameters nozzle diameter and layer height. The smaller these parameters are, the greater is the number of pores and the smaller is the pore size introduced into the mesostructure; the ductility of the FFF ABS part is remarkably enhanced.

## Funding Sources

This research is financially supported by Sächsische Aufbaubank by tax funds on the basis of the budget adopted by the deputies of the Saxon state parliament in Germany. The project “Etablieren eines Kompetenzfeldes Additive Fertigung plus an der Berufsakademie Sachsen” has the application number: 100395564.

## CRedit authorship contribution statement

**Dirk Fischer:** Writing - Experimental setup, Experimental work, Experimental data analysis. **Nickel Daniela:** Writing – review & editing, Project administration, Methodology, Formal analysis, Conceptualization. **Dietrich Dagmar:** Writing – review & editing, Methodology. **Schönherr Robert:** Formal analysis, Conceptualization. **Eßbach Claudia:** Writing – review & editing, Formal analysis, Data curation.

## Declaration of Competing Interest

The authors declare that they have no known competing financial interests or personal relationships that could have appeared to influence the work reported in this paper.

## Acknowledgements

We thank Prof. Dr. Frauke Deckow and Dr. Matthias Rößler from Berufsakademie Sachsen – Staatliche Studienakademie Glauchau for administrative support. We also thank Wolfgang Förster, Elke Rüprich, Ruben Mühlhans, Denis Freudenberg, Falk Puschmann, Peter Neumann and Prof. Dr. Thomas Pucklitzsch from Berufsakademie Sachsen – Staatliche Studienakademie Glauchau and Andreas Sedner from West-sächsische Hochschule Zwickau for valuable discussions and technical support.

## References

- U. Berger, A. Hartmann, D. Schmid, 3D-Druck - additive Fertigungsverfahren: Rapid Prototyping, Rapid Tooling, Rapid Manufacturing, third, Auflage, Verlag Europa-Lehrmittel Nourney, Vollmer GmbH & Co. KG, Haan-Gruiten, (2019).
- S. Upcraft, R. Fletcher, The rapid prototyping technologies, Assem. Autom. 23 (2003) 318–330, <https://doi.org/10.1108/01445150310698634>.
- J.R.C. Dizou, A.H. Espera, Q. Chen, R.C. Advincula, Mechanical characterization of 3D-printed polymers, Addit. Manuf. 20 (2018) 44–67, <https://doi.org/10.1016/j.addma.2017.12.002>.
- C. Bonten, Kunststofftechnik: Einführung und Grundlagen, third., aktualisierte Auflage, Hanser, München, (2020).
- M.S. Agerer, Kunststoff ABS - Acrylnitril-Butadien-Styrol, (2021). (<https://www.maschinenebau-wissen.de/skript3/werkstofftechnik/kunststoffe/356-abs>).
- T. Seul, S. Roth (Eds.), Kunststoffe in der Medizintechnik: Vorschriften und Regularien, Produktrealisierung, Herstellungsprozesse, Qualifizierungs- und Validierungsstrategien, Hanser, München, (2020).
- M. Helbig, Mehrskalenmodellierung von Schädigung in Gummimodifizierten Thermoplastischen Kunststoffen, KIT Scientific Publishing, 2018.
- A. Detailed, Guide on Acrylonitrile Butadiene Styrene, 8th, (2021). (<https://omnexus.specialchem.com/selection-guide/acrylonitrile-butadiene-styrene-abs-plastic/key-applications>) (Accessed 8th Dec. 2021).
- C.R. Bernal, P.M. Frontini, M. Sforza, M.A. Bibbó, Microstructure, deformation, and fracture behavior of commercial ABS resins, J. Appl. Polym. Sci. 58 (1995) 1–10, <https://doi.org/10.1002/app.1995.070580101>.
- D.H. Ramezani, F. Barbe, L. Delbreilh, M.B. Azzouna, A. Guillet, T. Breteau, Polymer additive manufacturing of ABS structure: influence of printing direction on mechanical properties, J. Manuf. Process. 44 (2019) 288–298, <https://doi.org/10.1016/j.jmapro.2019.06.015>.
- A.K. Sood, R.K. Ohdar, S.S. Mahapatra, Parametric appraisal of mechanical property of fused deposition modelling processed parts, Mater. Des. 31 (2010) 287–295, <https://doi.org/10.1016/j.matdes.2009.06.016>.
- C. Eßbach, D. Fischer, D. Nickel, Challenges in electroplating of additive manufactured ABS plastics, J. Manuf. Process. 68 (2021) 1378–1386, <https://doi.org/10.1016/j.jmapro.2021.06.037>.
- J.M. Chacón, M.A. Caminero, E. García-Plaza, P.J. Núñez, Additive manufacturing of PLA structures using fused deposition modelling: effect of process parameters on mechanical properties and their optimal selection, Mater. Des. 124 (2017) 143–157, <https://doi.org/10.1016/j.matdes.2017.03.065>.
- A.C. Abbott, G.P. Tandon, R.L. Bradford, H. Koerner, J.W. Baur, Process-structure-property effects on ABS bond strength in fused filament fabrication, Addit. Manuf. 19 (2018) 29–38, <https://doi.org/10.1016/j.addma.2017.11.002>.
- B.M. Tymrak, M. Kreiger, J.M. Pearce, Mechanical properties of components fabricated with open-source 3-D printers under realistic environmental conditions, Mater. Des. 58 (2014) 242–246, <https://doi.org/10.1016/j.matdes.2014.02.038>.
- W. Wu, P. Geng, G. Li, Di Zhao, H. Zhang, J. Zhao, Influence of layer thickness and raster angle on the mechanical properties of 3D-Printed PEEK and a comparative mechanical study between PEEK and ABS, Materials 8 (2015) 5834–5846, <https://doi.org/10.3390/ma8095271>.
- G.C. Onwubolu, F. Rayegani, Characterization and optimization of mechanical properties of ABS parts manufactured by the fused deposition modelling process, Int. J. Manuf. Eng. 2014 (2014) 1–13, <https://doi.org/10.1155/2014/598531>.
- N. Mosleh, A.M. Rezadoust, S. Darioush, Determining process-window for manufacturing of continuous carbon fiber-reinforced composite Using 3D-printing, Mater. Manuf. Process. 36 (2021) 409–418, <https://doi.org/10.1080/10426914.2020.1843664>.
- K.A. Al-Ghamdi, Sustainable FDM additive manufacturing of ABS components with emphasis on energy minimized and time efficient lightweight construction, Int. J. Lightweight Mater. Manuf. 2 (2019) 338–345, <https://doi.org/10.1016/j.ijlmm.2019.05.004>.
- B. Rankouhi, S. Javadpour, F. Delfanian, T. Letcher, Failure analysis and mechanical characterization of 3D printed ABS with respect to layer thickness and orientation, J. Fail. Anal. Prev. 16 (2016) 467–481, <https://doi.org/10.1007/s11668-016-0113-2>.
- F. Rayegani, G.C. Onwubolu, Fused deposition modelling (FDM) process parameter prediction and optimization using group method for data handling (GMDH) and differential evolution (DE), Int. J. Adv. Manuf. Technol. 73 (2014) 509–519, <https://doi.org/10.1007/s00170-014-5835-2>.
- J. Lluch-Cerezo, R. Benavente, M.D. Meseguer, S.C. Gutiérrez, Study of samples geometry to analyze mechanical properties in Fused Deposition Modeling process (FDM), Procedia Manuf. 41 (2019) 890–897, <https://doi.org/10.1016/j.promfg.2019.10.012>.
- S.-H. Ahn, M. Montero, D. Odell, S. Roundy, P.K. Wright, Anisotropic material properties of fused deposition modeling ABS, Rapid Prototyp. J. 8 (2002) 248–257, <https://doi.org/10.1108/13552540210441166>.
- M. Dawoud, I. Taha, S.J. Ebeid, Mechanical behaviour of ABS: an experimental study using FDM and injection moulding techniques, J. Manuf. Process. 21 (2016) 39–45, <https://doi.org/10.1016/j.jmapro.2015.11.002>.
- W. Zhang, A.S. Wu, J. Sun, Z. Quan, B. Gu, B. Sun, C. Cotton, D. Heider, T.-W. Chou, Characterization of residual stress and deformation in additively manufactured ABS polymer and composite specimens, Compos. Sci. Technol. 150 (2017) 102–110, <https://doi.org/10.1016/j.compscitech.2017.07.017>.
- E. Kim, Y.-J. Shin, S.-H. Ahn, The effects of moisture and temperature on the mechanical properties of additive manufacturing components: fused deposition modeling, Rapid Prototyp. J. 22 (2016) 887–894, <https://doi.org/10.1108/RPJ-08-2015-0095>.
- F. Saenz, C. Otarola, K. Valladares, J. Rojas, Influence of 3D printing settings on mechanical properties of ABS at room temperature and 77 K, Addit. Manuf. 39 (2021), 101841, <https://doi.org/10.1016/j.addma.2021.101841>.
- A. Vairis, M. Petousis, N. Vidakis, K. Savvakis, On the strain rate sensitivity of Abs and Abs plus fused deposition modeling parts, J. Mater. Eng. Perform. 25 (2016) 3558–3565, <https://doi.org/10.1007/s11665-016-2198-x>.
- N. Vidakis, M. Petousis, A. Vairis, K. Savvakis, A. Maniadis, A parametric determination of bending and Charpy's impact strength of ABS and ABS-plus fused deposition modeling specimens, Prog. Addit. Manuf. 4 (2019) 323–330, <https://doi.org/10.1007/s40964-019-00092-8>.
- INEOS Styrolution Europe GmbH, Datasheet of Terluran® GP-35, (2021). (<https://www.campusplastics.com/campus/de/datasheet/Terluran%C2%AE+GP-35/INEOS+Styrolution/654/d4a7a7cd/SI?pos=437>).
- A. En-naji, N. Mouhib, H. Farid, M. El Ghorba, Prediction of thermomechanical behavior of acrylonitrile butadiene styrene using a newly developed nonlinear damage-reliability model, Frat. Ed. Integr. Strutt. 13 (2019) 748–762, <https://doi.org/10.3221/IGF-ESIS.49.67>.
- S. Fatima, W. Achraf, K. Abdelkarim, C. Hamid, E. Mohamed, Failure analysis of Acrylonitrile Butadiene Styrene (ABS) materials and damage modeling by fracture, Int. J. Perform. Eng. 15 (2019) 2285, <https://doi.org/10.23940/ijpe.19.09.p1.22852293>.
- F. Ezzahra Nassih, A. Wahid, S. Fatima, C. Hamid, E. Mohamed, Reliability estimation of acrylonitrile butadiene styrene based on cumulative damage, Int. J. Perform. Eng. 16 (2020) 702, <https://doi.org/10.23940/ijpe.20.05.p3.702710>.
- V.E. Kuznetsov, A.N. Solonin, O.D. Urzhumtsev, R. Schielling, A.G. Tavtov, Strength of PLA components fabricated with fused deposition technology using a

- desktop 3D printer as a function of geometrical parameters of the process, *J. Mater. Sci. Eng.* 07 (2018), <https://doi.org/10.4172/2169-0022.1000429>.
- [35] G. Sie, The Olsson Block - a community invention by Anders Olsson, (2015). (<https://ultimaker.com/learn/the-olson-block-a-community-invention-by-anders-olsson>).
- [36] P. Wang, B. Zou, H. Xiao, S. Ding, C. Huang, Effects of printing parameters of fused deposition modeling on mechanical properties, surface quality, and microstructure of PEEK, *J. Mater. Process. Technol.* 271 (2019) 62–74, <https://doi.org/10.1016/j.jmatprotec.2019.03.016>.
- [37] S. Garzon-Hernandez, D. Garcia-Gonzalez, A. Jérusalem, A. Arias, Design of FDM 3D printed polymers: an experimental-modelling methodology for the prediction of mechanical properties, *Mater. Des.* 188 (2020), 108414, <https://doi.org/10.1016/j.matdes.2019.108414>.
- [38] DIN Deutsches Institut für Normung e.V, Plastics – determination of tensile properties – part 1: general principles (ISO 527-1:2019); German version EN ISO 527-1:2019, 1st ed., Beuth Verlag GmbH, 10772 Berlin ICS 83.080.01, (2019).
- [39] DIN Deutsches Institut für Normung e.V, Plastics – determination of tensile properties – part 2: test conditions for moulding and extrusion plastics (ISO 527-2: 2012); German version EN ISO 527-2:2012, 2nd ed., Beuth Verlag GmbH, 10772 Berlin ICS 83.080.01, (2012).
- [40] C. Abeykoon, P. Sri-Amphorn, A. Fernando, Optimization of fused deposition modeling parameters for improved PLA and ABS 3D printed structures, *Int. J. Lightweight Mater. Manuf.* 3 (2020) 284–297, <https://doi.org/10.1016/j.ijlmm.2020.03.003>.
- [41] H.I. Medellin-Castillo, J. Zaragoza-Siqueiros, Design and manufacturing strategies for fused deposition modelling in additive manufacturing: a review, *Chin. J. Mech. Eng.* 32 (2019), <https://doi.org/10.1186/s10033-019-0368-0>.
- [42] F. Zwicky, Morphologische Forschung: Wesen und Wandel materieller und geistiger struktureller Zusammenhänge, second. Aufl., Baeschin, Glarus, (1989).
- [43] P. Naefe, Methodisches Konstruieren, Springer Fachmedien Wiesbaden, Wiesbaden, 2018.
- [44] M. Kumke, Methodisches Konstruieren von Additiv Gefertigten Bauteilen, Springer Fachmedien Wiesbaden, Wiesbaden, 2018.
- [45] R.P. Kambour, A review of crazing and fracture in thermoplastics, *J. Polym. Sci. Macromol. Rev.* 7 (1973) 1–154, <https://doi.org/10.1002/pol.1973.230070101>.
- [46] C.B. Bucknall, R.R. Smith, Stress-whitening in high-impact polystyrenes, *Polymer* 6 (1965) 437–446, [https://doi.org/10.1016/0032-3861\(65\)90028-5](https://doi.org/10.1016/0032-3861(65)90028-5).
- [47] R.S. Moore, C. Gieniewski, Rheo-optical properties of ABS polymers and their component materials, *J. Appl. Phys.* 41 (1970) 4367–4374, <https://doi.org/10.1063/1.1658469>.
- [48] J. Williams, The difference between knit and meld lines—and why it matters, (2020). (<https://www.ptonline.com/articles/the-difference-between-knit-and-meld-lines-and-why-it-matters>).
- [49] C. McIlroy, P.D. Olmsted, Disentanglement effects on welding behaviour of polymer melts during the fused-filament-fabrication method for additive manufacturing, *Polymer* 123 (2017) 376–391, <https://doi.org/10.1016/j.polymer.2017.06.051>.
- [50] I. Calafel, R.H. Aguirresarobe, M.I. Peñas, A. Santamaría, M. Tierno, J.I. Conde, B. Pascual, Searching for rheological conditions for FFF 3D printing with PVC based flexible compounds, *Materials* 13 (2020), <https://doi.org/10.3390/ma13010178>.
- [51] Team Softusvista, Young's Modulus of porous material calculator, (2021). (<https://www.calculatoratoz.com/en/youngs-modulus-of-porous-material-calculator/Calc-91?Formulaid=917>).
- [52] G.H. Michler, Modellierung des Einflusses des Kautschukgehaltes auf die Craze-Bildung in schlagzähnen Polymeren, *Acta Polym.* 36 (1985) 325–330, <https://doi.org/10.1002/actp.1985.010360607>.